




# Spectrally tunable liquid resonator based on electrowetting

WEI YANG LIM,<sup>1</sup>  MO ZOHRABI,<sup>2</sup> JIANGANG ZHU,<sup>2</sup> TOMER UR SOCO,<sup>3</sup> TAL CARMON,<sup>3</sup> JULIET T. GOPINATH,<sup>2,4,\*</sup>  AND VICTOR M. BRIGHT<sup>1</sup>

<sup>1</sup>*Department of Mechanical Engineering, University of Colorado, Boulder, Colorado 80309, USA*

<sup>2</sup>*Department of Electrical, Computer, and Energy Engineering, University of Colorado, Boulder, Colorado 80309, USA*

<sup>3</sup>*School of Electrical Engineering, Tel Aviv University, Tel Aviv 6997801, Israel*

<sup>4</sup>*Department of Physics, University of Colorado, Boulder, Colorado 80302, USA*

\**Juliet.gopinath@colorado.edu*

**Abstract:** We present a tunable on-chip liquid resonator in conjunction with a tapered fiber coupling scheme. The resonator consists of a glycerol droplet submerged within an immiscible liquid bath, which mitigates the effects of environmental fluctuations. The platform is fabricated using standard semiconductor techniques, which enable the future integration of photonic components for an on-chip liquid resonator device. The liquid resonator maintains its high Q-factor on chip ( $10^5$ ) due to surface tension forming an atomically smooth liquid-liquid interface. Higher Q-factor resonance modes experienced linewidth broadening due to the random excitation of thermal capillary vibrations. Spectral tuning is demonstrated using the electrowetting effect, increasing the surface's wettability and an expansion in the droplet diameter. A maximum spectral tuning of  $1.44 \text{ nm} \pm 5 \text{ pm}$  is observed by applying 35 V. The tuning range is twice the free spectral range (FSR) of 0.679 nm measured at a pumping wavelength range of 770-775 nm. A 2D axisymmetric finite-element simulation shows resonance modes in good agreement with experimentally measured spectra and with predicted tuning speeds of 20 nm/s.

© 2022 Optica Publishing Group under the terms of the [Optica Open Access Publishing Agreement](#)

## 1. Introduction

Whispering gallery mode (WGM) optical microresonators have attracted great interest due to the high-quality factor (Q-factor  $> 10^6$ ) and small mode volume. These qualities have enabled resonators to detect physical perturbations with high sensitivity [1–5] and access nonlinear optical phenomena [6–10] with high confined peak power. In a microresonator, only specific WGM resonance modes are permitted to propagate. These resonance modes are set by geometrical properties of the resonator and can be approximated using an explicit asymptotic solution to the Mie scattering theory [11,12]. While much consideration is taken in the design and fabrication of microresonators, unavoidable variabilities during the fabrication process can lead to the mismatch in cavity resonance such as in the case of quantum electrodynamic cavity applications [13]. As a result, tunability of the resonance modes is highly desirable to compensate for frequency mismatch, but also for a larger set of applications including microlasers [14–16], optical filters [17,18], and optical switches [19,20]. Ideally, tuning range for these applications would exceed the resonator's free spectral range (FSR) to freely access any resonance mode across the optical wavelength [21,22]. This condition is especially challenging in smaller resonators ( $r < 50 \mu\text{m}$ ) as the free spectral range (FSR) would exceed 1 nm [23]. Moreover, large tunability often induces asymmetry within the resonator leading to a degradation of the Q-factor. Numerous tuning techniques for rigid solid resonators have been proposed: inducing mechanical strain using a piezoelectric transducer [21,23,24], altering birefringence using nematic liquid crystal [25–27], and manipulating the refractive index through the thermo-optical effect [13,28]. These different

techniques come with tradeoffs, with mechanical strain requiring a complex external setup, liquid crystals suffering from low Q-factors, and the thermo-optic effect having a frequency response roll-off dependent on the surrounding environment. Instead, we look to explore the concept of a liquid droplet microresonator which can undergo large reversible deformation exceeding its FSR while maintaining a high Q-factor.

The concept of a liquid resonator has been around since the early days of optical resonator research [29–32] but remains largely unexplored in comparison to solid resonators. It has recently gained a resurgence of attention [16,33–43] due to interesting properties which are difficult to obtain in solid resonators [44]. Foremost, the liquid-liquid interface is formed by a balance of interfacial surface tension and internal pressure, which leads to an interface which is atomically smooth (surface roughness of only a few Angstroms [45]) in either the rest or actuated state. For systems where surface tension dominates over gravitational forces, the liquid's surface tension will minimize the surface area which results in the formation of an almost spherical droplet [46]. A recent study has illustrated this effect by levitating a liquid droplet which avoids dislocations or thermally induced stress typically present in solid resonators, resulting in a measured Q-factor of over a billion [47]. In general, the optical Q-factor in liquid resonators is limited primarily by material absorption and radiation loss [33] (due to the small refractive index contrast,  $\Delta n \approx 0.1$ – $0.2$ , with a surrounding liquid), in comparison to solid resonators where it is constrained by scattering loss. Due to the dynamic interplay between surface tension and pressure, a droplet can be geometrically altered to produce large spectral shifts ( $> 1$  nm) without inducing irreversible changes to its shape or cavity resonance frequency. Additionally, droplets ( $< 1$  mm) are able to respond to driving signal frequencies in the kHz regime [48,49]. The combination of these properties of a liquid resonator makes it an ideal solution for applications that require dynamic tuning.

Despite the exciting opportunities, liquid microresonators face challenges that constrain the more widespread adoption of the technology. The main issues stem from difficulty in integrating with existing semiconductor technologies, sensitivity to environmental humidity [34,50], optocapillary noise [51], radiation pressure broadening ( $\sim 10$  pm) [52], and optoacoustic oscillations [53]. Vahala and Hossein-Zadeh demonstrate an efficient light coupling to a water droplet surrounded by another liquid using tapered fiber [54]. Kiraz *et al.* show spectral tuning of standalone liquid microdroplets on a superhydrophobic surface using electrowetting [55]. Recently, Zheng *et al.* demonstrate a tunable bragg grating filter based on liquid droplet sagging on a superhydrophobic surface [42]. In this work, we introduce an on-chip platform for liquid resonators which maintains a high Q-factor ( $10^5$ ) and provides control over the cavity resonance using the electrowetting-on-dielectric effect. The device is fabricated using standard semiconductor fabrication techniques which allows for future integration of photonic components such as waveguides, on-chip laser source, or potentially a microfluidic system for droplet generation and sensing. The liquid microresonator consists of a glycerol droplet, positioned on a hydrophobic surface, submerged within an immiscible liquid bath (dodecane or hexane). Humidity and vibrational effects are suppressed with the surrounding liquid but can be further improved by fully packaging the device. A light is coupled to the resonator using tapered fiber. Spectral tunability of the liquid resonator is achieved by applying an electric potential causing the radial diameter of the droplet to expand and the red shift in resonance frequency. A geometrical analysis on the actuation of the liquid droplet is performed using the Lippmann-Young electrowetting equation and compared to the experimental results. In addition, the mode profile and resonance mode frequencies are simulated by coupling the laminar two-phase liquid flow physics and wave-optics in COMSOL Multiphysics, confirming the resonance tuning observed in the experiment. Lastly, we have observed higher Q-factor resonance modes. However, these resonances experienced broadening due to thermal capillary noise at higher optical powers. We

have solved the optical rate and heat equations numerically and the results agree well with our experimental findings.

## 2. Electrowetting in a liquid resonator

The electrowetting effect is the change in wettability of a surface through an applied electric field [56]. The effect is first described by Gabriel Lippmann and has been gaining popularity over the past decade as an efficient and simple method to manipulate liquids [57–61]. A typical electrowetting design is analogous to a parallel plate capacitor. An electric potential is applied across two electrodes with an insulating layer separating the liquid from either one or both the electrodes. The insulator acts as a separation barrier to prevent charge or ion transfer and issues with electrolysis. In the presences of an electric field, electrical charges buildup along the electrode side of the insulator, while dissolved counter ions ( $H^+$  or  $OH^-$  in water) within the liquid accumulate on the solid-liquid interface to form an electrical double layer [57]. Based on Gibbsian interfacial thermodynamics, it can be then shown that the increase in surface charge density leads to the effective reduction in the solid-liquid surface tension and contact angle of the liquid [57,62,63]. The liquid's contact angle response is described by the Lippmann-Young equation:

$$\cos(\theta_f) = \cos(\theta_i) + \frac{\epsilon_o \epsilon_r}{2d\gamma_{lf}} U^2, \quad (1)$$

where  $\theta_f$  represents the final contact angle of the droplet after actuation,  $\theta_i$  is the initial contact angle,  $\epsilon_o$  is the permittivity of free space,  $\epsilon_r$  is the dielectric constant of the insulator,  $d$  is the dielectric thickness,  $\gamma_{lf}$  is the interfacial surface tension between the liquid-surrounding fluid, and  $U$  is the applied voltage. For simplification, we introduce a constant  $\alpha = \cos(\theta)$  and a dimensionless electrowetting number  $\eta = (\epsilon_o \epsilon_r / 2d\gamma_{lf}) U^2$ . The value of  $\alpha$  is bounded between  $-1 \leq \alpha \leq 0$  with a lower limit of  $90^\circ$  contact angle which is required to confine the propagating light within a WGM resonator. The relationship between the applied voltage and the optical resonance shift can be derived through a geometrical approach. Initially, we consider a spherical surface geometry with an inherent contact angle with an initial volume of:

$$V = \frac{\pi r_i^3}{3} [2 + \alpha_i^3 - 3\alpha_i], \quad (2)$$

Here,  $r_i$  represents the initial radius of the droplet and  $\alpha_i / \alpha_f$  represent the cosine of the initial and final contact angle [see Fig. 1(a)]. For a WGM resonator droplet with a diameter of  $\sim 100$   $\mu\text{m}$ , the Bond number [57] ( $\Delta\rho g L^2 / \gamma$ ) is  $\sim 10^{-4} \ll 1$ . This indicates that the system is dominated by surface tension forces, justifying the assumption that the droplet is spherical in geometry and gravitational effect is negligible. By applying an electric potential, the contact angle of the droplet is reduced as depicted in Fig. 1(b) and the droplet achieves a new equatorial radius. Through the conservation of mass, the change in radius can be evaluated using Eqs. (1) and (2) by equating the volume before and after actuation [Eq. (1)].

$$\Delta r = r_i \left[ \frac{2 + \alpha_i^3 - 3\alpha_i}{2 + \alpha_f^3 - 3\alpha_f + \eta^3 + 3\eta^2\alpha_f + 3\eta(\alpha_f^2 - 1)} \right]^{\frac{1}{3}} - r_i, \quad (3)$$

Further simplification can be made as  $\eta \sim 10^{-2} \ll 1$  under the typical conditions for a microscale device ( $\epsilon_r = 2$ ,  $d = 1$   $\mu\text{m}$ ,  $\gamma_{lf} = 25$   $\text{mN/m}$ ,  $U = 10$   $\text{V}$ ) and the higher order  $\eta$  terms become negligible. As the terms  $(\alpha_f^2 - 1) \leq 0$  and  $\eta > 0$ , increasing the applied voltage would lead to the reduction of the denominator and an overall expansion of the radius. The optical resonance shift

is proportional to the geometrical change in radius of the resonator, which yields [1,64]:

$$\Delta\lambda = \lambda_o \left[ \frac{2 + \alpha_i^3 - 3\alpha_i}{2 + \alpha_f^3 - 3\alpha_f + 3\eta(\alpha_f^2 - 1)} \right]^{\frac{1}{3}} - \lambda_o, \quad (4)$$

where  $\lambda_o$  is the optical wavelength in vacuum. The resonance is expected to redshift with electrowetting actuation due to the increase in the resonator radius. The derived relationship avoids the small angle approximation [55] and can be applied as long as the contact angle follows the Lippmann-Young's equation (before the onset of contact angle saturation). Under such a design, a droplet with a contact angle of  $150^\circ$  would exhibit 1.9 nm wavelength shift with 10 V. However, if the microresonator is driven at higher voltages, the higher order  $\eta$  terms cannot be neglected. It is worth noting that the droplet is being actuated asymmetrically, which will cause a slight shift in the height of equatorial plane. This effect can be suppressed by sandwiching the droplet between a second surface and applying potential between both surfaces. For experimental simplicity, we chose a single surface electrowetting design.

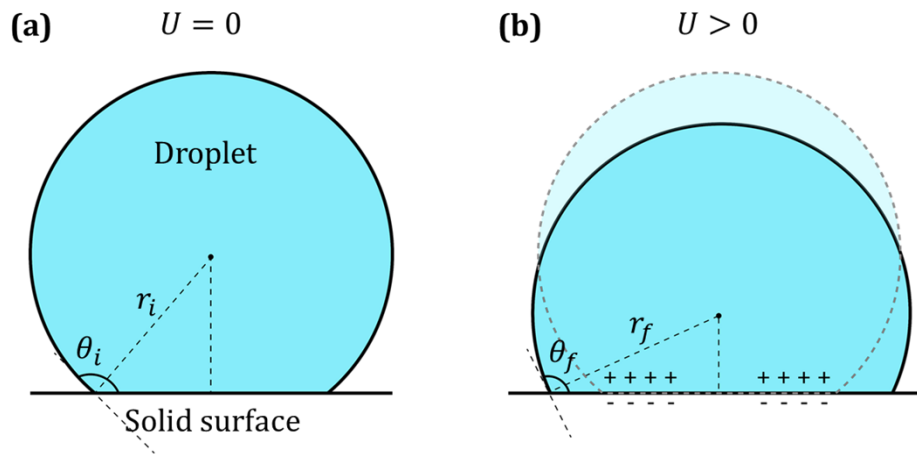


**Fig. 1.** (a) Geometry of a liquid droplet resting on top of a dielectric solid surface with an initial contact angle of  $\theta_i$  and a radius of  $r_i$ . (b) When an electrical potential ( $U$ ) is applied to droplet, charges buildup underneath the dielectric surface and ions within the droplet accumulate on the other side of the dielectric surface. This leads to a decrease in the solid-liquid surface tension and an expansion in equatorial radius ( $r_f$ ).

### 3. Device fabrication and experimental setup

The tunable microresonator is fabricated using standard microfabrication techniques, which integrate the electrodes necessary for electrowetting and provide a hydrophobic surface for the droplet [ Fig. 2]. The process begins with the evaporation and patterning of the ground electrode on a fused silica wafer (300 nm Au and 20 nm Ti adhesion layer) [Fig. 2(a)]. In Fig. 2(b), a  $12.2 \mu\text{m}$  layer of SU-8, chosen for its excellent physical properties and chemical resistance, is deposited on top of the ground electrode. Next, 300 nm of Al electrode is sputter deposited and patterned [Fig. 2(c)]. The SU-8 layer in between the two layers of electrodes is important because it enables an annular electrode design without any discontinuity in electrical connections near the liquid droplet. Additionally, a “well” shaped pattern is placed at the center to provide additional confinement to resist droplet motion during the filling of the bath. To prevent the conductive liquid from shorting the two actuating electrodes, a layer of dielectric (Parylene HT) is deposited

uniformly throughout using a physical vapor deposition method [Fig. 2 (d)]. The wafer is then diced into individual chips before a hydrophobic coating (Cytop) is spin coated onto individual chips [Fig. 2(e)]. Although Parylene HT is hydrophobic, the addition of Cytop enhances the initial contact angle of the liquid resonator droplet. The chip is attached to a custom printed circuit board (PCB) using a UV curable epoxy (Norland UVS-91) [Fig. 2(f)]. Electrical pads on the chip are wire bonded to the gold pads on the PCB for external connections [Fig. 2(g)]. Finally, the microresonator chip is secured inside the stainless-steel liquid holder before a droplet of glycerol ( $n = 1.47$ ) is dispensed onto the SU-8 well structure using a glass capillary tube [Fig. 2(f)].

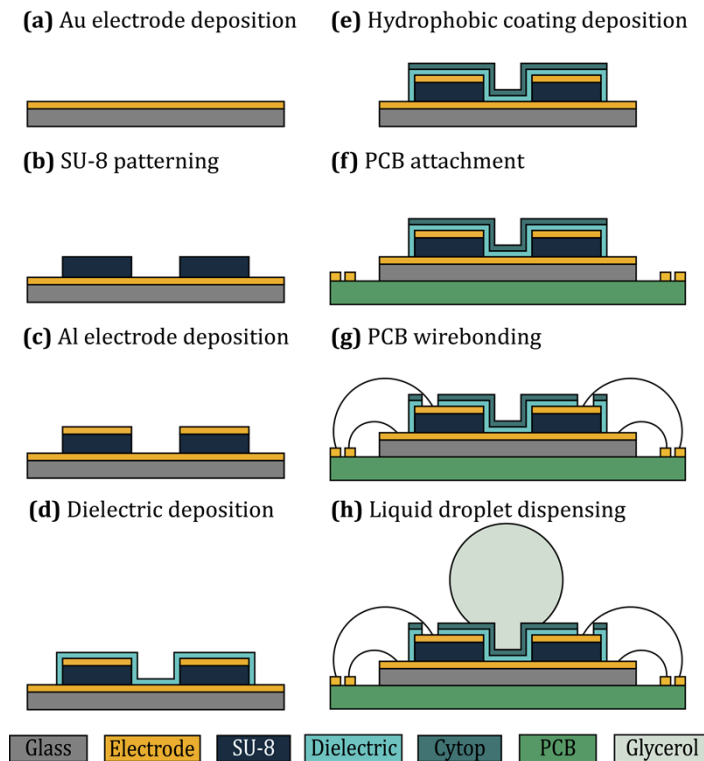


**Fig. 2.** Fabrication process illustration of the liquid microresonator chip. (a) Gold electrodes are patterned on a fused silica wafer. (b) A permanent SU-8 photoresist is patterned to create a “well” shape design and an elevated layer for the subsequent annular electrode. (c) Aluminum electrodes are sputtered onto the SU-8 layer and patterned. (d) The Parylene HT dielectric is uniformly deposited using physical vapor deposition. (e) Individual chips are diced from the wafer and a hydrophobic coating is spin coated onto the chip. (f) Microresonator chip is epoxy bonded to the PCB. (g) Electrical pads are exposed, and wire bonded to the PCB for external electrical connections. (f) The chip is attached inside of a stainless-steel bath holder before a droplet of glycerol is dispensed using a glass micropipette and submerged within an immiscible liquid surrounding.

The schematic of the optical setup is depicted in Fig. 3. A tunable, single-frequency, continuous wave laser (765–781 nm – Newport TLB 6712) is coupled to a single mode fiber (Thorlabs SM600). One percent of the laser power is split and continuously monitored before the tapered fiber, while the transmission signal is recorded on a fast photodetector (Newport 1801-FC) with a bandwidth of 125 MHz. The tapered fiber is fabricated using the heat-and-pull method to

achieve a final waist diameter of  $\sim 1\text{-}2\ \mu\text{m}$  with a transmission of over 95% in best outcomes. The heat source used is based on a custom ceramic heater design [65] where electrical resistive wire is coiled around a ceramic tube which maintains a consistent temperature. Dimensions of the ceramic tube is kept small (13 mm length and 9.5 mm diameter) and clamped in between calcium silicate plates with low thermal conductivity which enabled temperatures of  $\sim 1200\ \text{°C}$  to be reached with 150 W. Both temperature and tapering speed are important parameters to consider, as non-adiabatic tapering occurs if the speed is too fast and or the fiber sagging under its own weight if the temperature is too high. Tapered fiber produced is then clamped onto a machined fiber holder and transferred to the experimental setup [see Fig. 4]. A side camera with a 10x objective images the droplet through a transparent window on the side of the liquid holder. The liquid holder is cleaned using isopropanol alcohol and ultrasonic agitation prior to attaching the microresonator chip. The glycerol droplet is then carefully dispensed onto the center of the electrode pad using a glass micropipette before the surrounding non-polar liquid dodecane ( $n = 1.42$ ) or hexane ( $n = 1.375$ ) is pipetted into the bath until the droplet is completely submerged. A cover is placed over the bath to prevent debris from contaminating the bath. The droplet diameter is measured to be  $191\ \mu\text{m}$  with an initial contact angle of  $145.8 \pm 1.8^\circ$  through the side camera (Fig. 5).

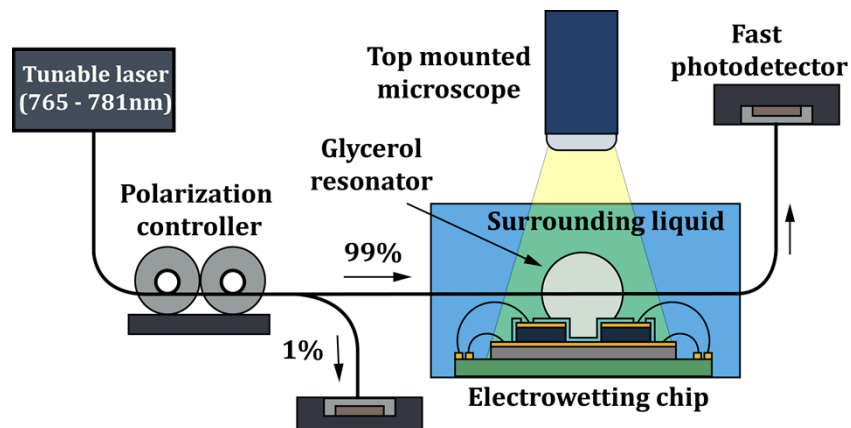


**Fig. 3.** Schematic of the liquid microresonator experimental setup. Light is coupled into the liquid droplet microresonator through a tapered fiber positioned along the equatorial plane of the droplet. The tunable laser is swept across a spectral range (770-775 nm), while a fast photodetector records the transmission spectra.

The tapered fiber is coupled to the glycerol droplet along the equatorial plane of the droplet during the tuning experiments.

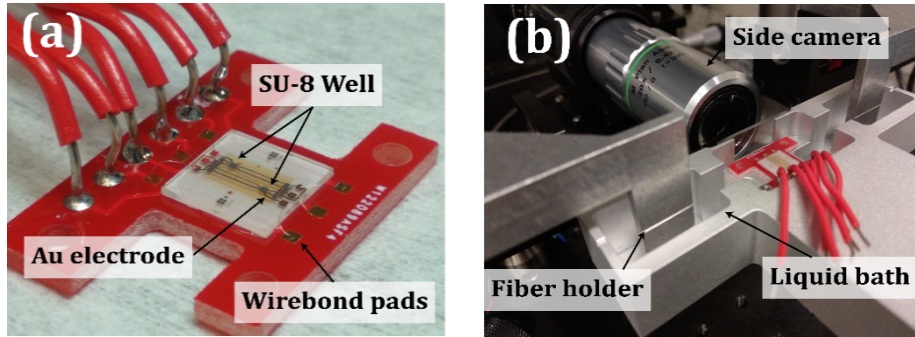


**Fig. 4.** (a) Assembled tunable microresonator chip with electrowetting electrodes connected to a custom printed circuit board. The SU-8 wells are situated to enable the individual coupling of each droplet and the imaging of the droplet through the side camera. (b) Fiber holder on each side contains a v-shaped groove for fiber alignment, while magnets hold the tapered fiber in place. The stainless-steel bath holds the microresonator chip within a liquid bath of dodecane. The liquid bath is raised into coupling height using a Thorlabs Nanomax positioning stage.

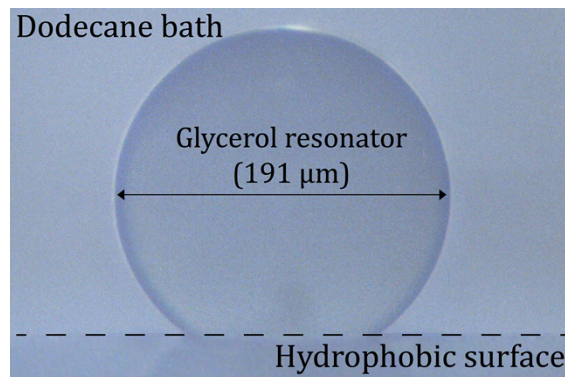


**Fig. 5.** Side view image of a glycerol liquid droplet on the electrowetting chip surrounded by a dodecane bath. Dashed line indicates the surface of the chip. Initial contact angle is measured at  $145.8^\circ$  with a diameter of  $191 \mu\text{m}$ .

#### 4. Experimental results

The tunable laser is scanned across a wavelength of 770 to 775 nm, using an external function generator at a rate of 0.25 nm/s. An initial baseline of the transmission spectra is collected before the fiber is moved into coupling distance of the liquid resonator. When the laser matches the optical resonance frequency, light is coupled into the droplet resulting in a transmission power drop. The Q-factor of the glycerol-dodecane liquid system is measured using a Lorentzian curve which yields  $4 \times 10^4$  [ Fig. 6]. The theoretical limit of the system's Q-factor is calculated analytically from Maxwell's equations [66] which identify the absorption-limited Q-factor for glycerol and dodecane to be  $\sim 10^7$ , with the radiation Q-factor slightly higher than experimental ( $\sim 10^5$ ). While radiation loss is typically negligible in resonators at this size ( $r_i \gg \lambda_o$ ), the low refractive index contrast between the droplet and surrounding liquid contributes to the poor confinement of the optical mode [54,67]. A non-polar liquid with a lower refractive index, such as hexane ( $n = 1.375$ ), can be used instead of dodecane for an improvement in refractive index contrast. The substitution increases the theoretical radiation Q-factor to  $7 \times 10^{13}$ , whereby the system is now absorption-limited by glycerol and the surrounding liquid. However, accessing the higher Q-factors presents additional challenges with radiation pressure induced noise discussed at the end of the section.

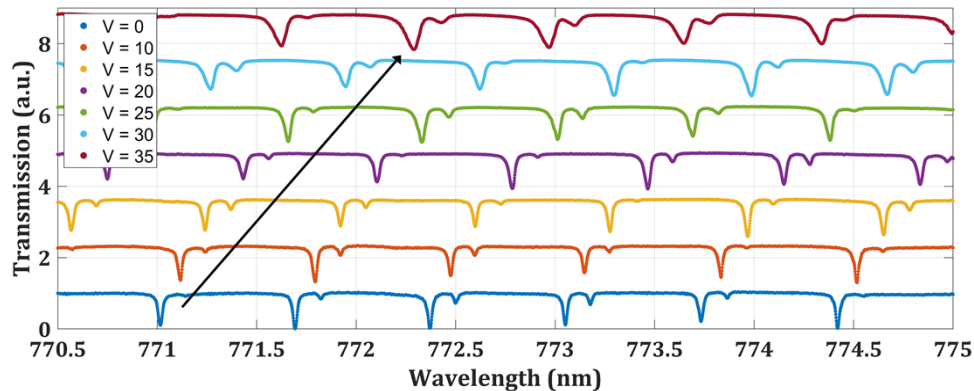


**Fig. 6.** Recorded transmission signal as a function of actuating voltage on a glycerol droplet surrounded by dodecane. The two peaks repeated across the spectra correspond to resonance modes of TM and TE polarization. When a sinusoidal voltage function is applied, the resonance frequency redshifts in agreement with the theoretical prediction and numerical simulation. Free spectral range is measured at 0.679 nm.

Due to the hygroscopic nature of glycerol, the droplet expands or contracts as it reacts to localized changes in humidity and temperature. This results in the drifting of resonance frequency and coupling position over time, eventually causing the droplet to come in contact with the fiber. By submerging the droplet within a surrounding liquid, the fluctuations are suppressed and provide several key advantages. Firstly, the contact angle of glycerol on the hydrophobic coating is  $\sim 100^\circ$ , which improves to  $145.8^\circ$  in a dodecane bath [see Fig. 5]. This enhancement of the curvature of the liquid resonator results in better light confinement and permits the use of a larger variety of liquid combinations. In addition, it raises the equatorial plane of the resonator, relaxing the tolerance for alignment, such that coupling with the tapered fiber can be done without contacting the edge of the chip. Secondly, optoacoustic oscillations are avoided due to the low acoustic impedance contrast between the two liquids resulting in the leakage of sound waves into the surrounding environment [68]. Finally, mechanical vibrational noise in the liquid resonator is reduced with the increased damping from the surrounding fluid (dodecane viscosity = 1.36 mPa·s, glycerol = 1412 mPa·s) [69,70].



In Fig. 6, two resonance modes are observed to be repeated across the scan. The free spectral range between successive modes is measured to be 0.679 nm, consistent with the measured droplet diameter of 191  $\mu\text{m}$ . As described by Lam *et al.* [11], the spectral position of the resonance can be estimated using the characteristics mode number with an explicit asymptotic formula without solving the standard Mie scattering formalism. Using the material parameters ( $n_{\text{glycerol}} = 1.47$ ,  $n_{\text{dodecane}} = 1.42$ ,  $r = 95.5 \mu\text{m}$ ), the predicted spectrum is found to match well with the observed results with deviations in spectral position of less than 10 pm. The two peaks correspond to the transverse electric (TE) and transverse magnetic (TM) fields with the TE modes resonating at longer wavelengths. When an electrical potential is applied to the microresonator chip at intervals of 5 V from 0 to 35 V, the resonance peaks redshift in agreement with theoretical predictions and the numerical simulation [Section 4]. Figure 7 illustrates the resonance shift as function of actuating voltage. A maximum spectral tuning of 1.44 nm is observed when 35 V is applied. Resonance shifts at the different voltage intervals are consistent across repeated scans with a standard deviation of 5 pm. With a tuning range larger than the mode FSR, the resonance can be adjusted to match any optical frequency. Q-factor broadening is observed at higher voltages due to the increased eccentricity of the resonator from asymmetrical actuations [55]. The asymmetry is likely caused by non-uniform actuation, either from localized surface roughness or uneven thickness of the dielectric, which distorts the spherical shape of the droplet. We found that the derived Eq. (4) fit well to the experimentally results with the initial contact angle and dimensionless electrowetting number used as fit parameters [see Fig. 7]. The initial contact angle obtained through the fitted equation is  $\sim 145.3^\circ$  which is within the uncertainty of the side camera measurements of  $145.8 \pm 1.8^\circ$ . The electrowetting constant ( $\epsilon_0 \epsilon_r / 2d \gamma_{lf}$ ) from the fitting is  $1.78 \times 10^{-5}$ . Using the permittivity of the dielectric and hydrophobic layer of  $\epsilon_r = 2.2$  and assuming  $d = 18 \mu\text{m}$ ,  $\gamma_{lf} = 25 \text{ mN/m}$  based on the geometry of the designed resonator, we obtain an electrowetting constant value of  $2.16 \times 10^{-5}$ . The calculated electrowetting constant is reasonably close to the experimentally observed value, but the slight discrepancy can be attributed to the uncertainty from the interfacial surface tension and the overall electric field distribution in the system. Overall, through the electrowetting equation, the applied voltage of 35 V resulted in a contact angle change of  $2.6^\circ$ .

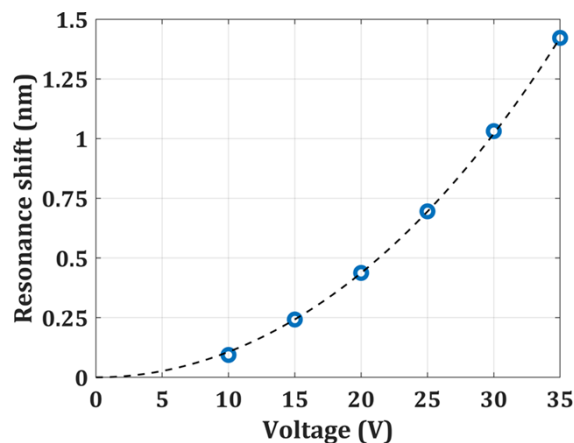


**Fig. 7.** Resonance wavelength tuning with electrowetting showing a maximum spectral tuning of 1.44 nm. The dash line shows a fit of the derived resonance shift [Eq. (4)] to the experimental data, obtaining the coefficients  $\alpha$  and  $\eta$ .

In efforts to improve the radiation Q-factor, the dodecane surrounding is replaced with a lower refractive index liquid, hexane. With the new liquid system, phase matching conditions

must still be satisfied to enable efficient coupling into the fundamental order modes [71]. The fiber's effective mode index in hexane is thus modeled using COMSOL Multiphysics and the fiber diameter ( $\sim 1.8 \mu\text{m}$ ) adjusted accordingly to the size of the droplet. The glycerol-hexane system saw improvements in the intrinsic Q-factors with multiple resonance peaks measuring  $\sim 1.06 \times 10^5$  [ Fig. 8]. At the same time, resonances with significant broadened lineshape and increased noise are observed [ Fig. 9]. The upscan transmission spectrum (laser swept from a lower wavelength) shown in Fig. 9 is obtained using  $\sim 1 \text{ mW}$  of optical power to illustrate the broadening effect (linewidth  $\sim 30 \text{ pm}$ ), but the effect could be observed at  $50 \mu\text{W}$  with a smaller linewidth ( $\sim 4 \text{ pm}$ ). The cavity resonance drifts as the pump frequency approaches the resonance frequency, causing a broadening in the spectrum [72]. Unlike the asymmetrical thermal broadening when the pump approaches from the red and blue detuned side, typically observed in solid resonators, a similar broadened spectrum is also observed during the downscan in this two liquid system. This suggests that additional effect of thermal capillary vibrations is preferentially blue shifting of the resonances. This differs from the observation reported in Ref. [52], in which asymmetrical linewidth broadening in the up- and down-scan due to radiation pressure was observed.

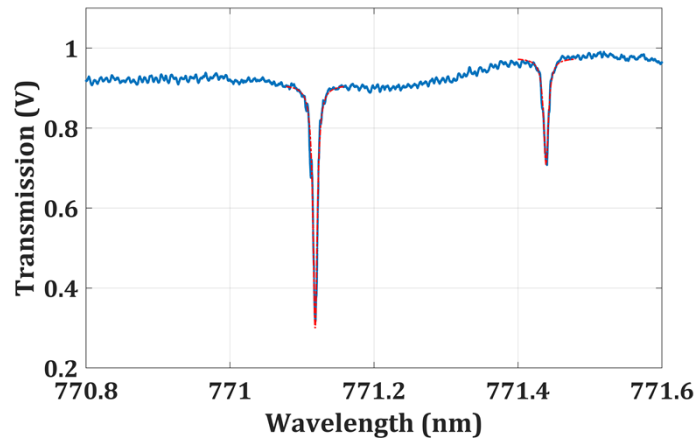


**Fig. 8.** Transmission spectra of the glycerol-hexane system ( $\Delta n = 0.095$ ) with multiple resonance peaks of  $\sim 1.06 \times 10^5$  Q-factors measured by fitting a Lorentzian function (red). Improvement in the Q-factor over the glycerol-dodecane system ( $\Delta n = 0.05$ ) is attributed to the increased refractive index contrast, reducing radiation losses.

The broadened spectra in both up and downscan is investigated by numerically calculating the spectral transition of the resonator. This is simulated using the material properties of glycerol with a specific heat capacity of  $2300 \text{ J}/(\text{kg}\cdot\text{K})$  and thermal conductivity of  $0.285 \text{ W}/(\text{m}\cdot\text{K})$ , to solve for the optical rate equation in the microresonators [73] [details in supplementary]. Detuning between the pump and the resonance frequency considers the additional effects of thermal expansion ( $4.5 \times 10^{-4} \text{ 1}/^\circ\text{K}$ ) [74], thermal optic coefficient ( $-2.3 \times 10^{-4} \text{ 1}/^\circ\text{C}$ ) [75], and a random noise function which simulates the thermal capillary vibrations of the droplet,  $\text{RN}(t) = \sum_{n=1}^3 a_n \sin(2\pi f_n t + \phi_n(t))$ . The relative amplitudes ( $a_n = \{1, 0.888, 0.805\}$ ) and frequencies ( $f_n = \{3184, 2488, 2786 \text{ Hz}\}$ ) of the first three dominant oscillations are obtained through the Fourier transform of the measured transmission spectrum depicted in Fig. 9.  $\phi_n(t)$  is the random phase term as a function of time ( $t$ ) simulating the random nature of the noise. From the numerical calculation, the random noise results in frequency detuning larger than the resonance's FWHM, which affects the system's behavior on either side of the resonance. In particular, when laser

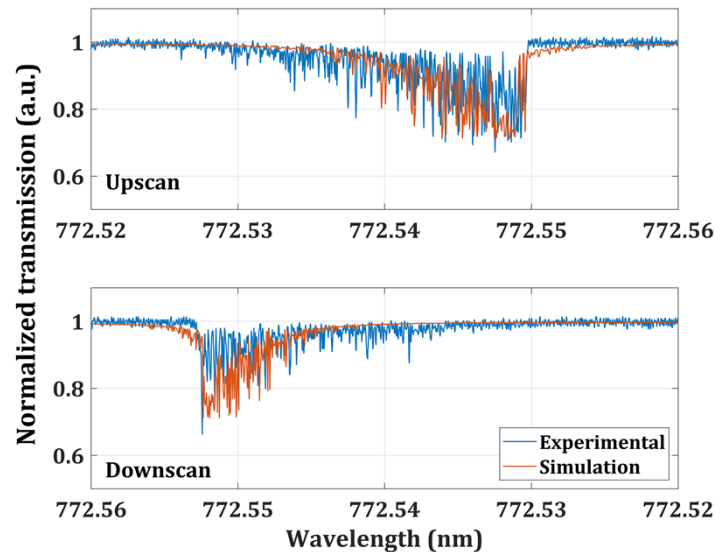


**Fig. 9.** High Q-factor resonance in glycerol-hexane liquid system displaying significant broadening during both the upscan, where the laser is swept from a lower to higher wavelength (top), and the downscan (bottom). The demonstrated spectrum is captured with  $\sim 1$  mW of power for better illustration of the broadening effect but remains present at  $50 \mu\text{W}$ . The thermal capillary noise results in random fluctuations. Furthermore, and quite unusually, lineshape broadening is relatively symmetric here, as evident from the shark tail shaped transmission that appears in both forward and backward scans, which is also resulting from thermal fluctuations.

frequency is, on average, at the resonator red detuned side, fluctuations can take the cavity to the other blue detuned side. When spending at the blue detuned side periods longer than the thermal time constant of the system, thermal drift can photothermally take the resonator to the blue detuned side. Switching to the blue detuned side is expected from the tendency of noise to take systems toward their stable equilibrium state, known in our case as the “thermal self-stability of microcavities” [72]; resulting in a relatively symmetrical broadening with nearly no hysteresis [Fig. 9].

In detail, when the laser is downscanned and the pump wavelength is higher than the resonance (on average), the randomness of the noise occasionally blue shifts the resonance, where the resonance can spend periods longer than the thermal time constant ( $136.2 \mu\text{s}$ ). Since the red detuned side is an unstable equilibrium [72], the resonance can switch sides, relative to the laser wavelength, not only temporarily but also on averaged, assisted by heating. The switch between the unstable red detuned side to the stable blue detuned side, is observed as a dip in the transmission which is present in both experimental and simulation results [Fig. 9]. To minimize the resonance broadening, the thermal time constant can be reduced by choosing a liquid with a better thermal conductivity and smaller heat capacity, increasing the interfacial surface tension, or reducing the input power.

## 5. Finite element simulations of resonator

We have performed two dimensional axisymmetric simulations using a finite element method (FEM) in COMSOL to investigate the electric field distributions and the resonance frequency mode of the liquid resonator under electrowetting actuation. The simulation utilizes the multiphysics modeling capability which combines the results from laminar flow computational fluid dynamics

(CFD) module with the wave optic module. We have numerically solved incompressible Navier-Stokes equations,  $\partial \vec{u} / \partial t + (\vec{u} \cdot \nabla) \vec{u} = \mu \nabla^2 \vec{u} - (1/\rho) \nabla p$  ( $\nabla \cdot \vec{u} = 0$ ), where  $\rho$  is the density of the fluid,  $\vec{u}$  is the velocity vector and  $p$  is the hydrodynamic fluid pressure. The simulation replicates the experimental condition of a 95.5  $\mu\text{m}$  radius glycerol droplet with an initial contact angle of  $\sim 145.8^\circ$ , surrounded by dodecane as shown in Fig. 5. The experimentally determined contact angle variation (electrowetting constant) is used at the contact point of the droplet and the substrate in the form of the Lippmann–Young’s equation. The outcome of the laminar flow simulation is the time-dependent wetting of the liquid droplet on the substrate to achieve a final contact angle based on the applied voltages. We have coupled the CFD solution to evaluate the optical resonance mode frequencies at each final contact angle (actuating voltage). To do so, refractive index of dodecane has been determined using a Metricon 2010/M prism coupler refractometer [76], while Glycerol has been measured previously in the literature using standard Abbe refractometer [77]. The refractive index of both liquids is evaluated by fitting to the Sellmeier equation as a function of wavelength to compute for the material dispersion.

The COMSOL wave-optic module allows for accurate determination of the time response, resonance frequencies, and modal distributions in an axial-symmetric structure. Starting from a resting state and actuating with a step on voltage function of 35 V, the liquid droplet settles to within 2.5% of the actuated state ( $143.4^\circ$ ) within  $\sim 75$  ms. It should be noted that the liquid droplet will follow electrical signals with frequencies higher than the step on response, albeit with a reduction in tuning range. This can be improved by reducing the droplet size, optimizing the liquid viscosity, and introducing a shaped voltage function, which suppresses the mechanical oscillations occurring at the liquid interface and pushing towards kHz speeds [48,49,78]. Ultimately, the frequency response for the electrowetting based actuation is limited by the time dynamics of the charge accumulation and discharge [56]. In the case for the dodecane and glycerol liquid system, the high viscosity of the glycerol droplet results in an underdamped system which limits the tuning speed.

Figure 10 (a) shows the electric field distribution in the glycerol liquid resonator with a diameter of 191  $\mu\text{m}$  for TE and TM modes. The whispering gallery mode resonances can be characterized by a radial ( $n$ ), polar ( $l$ ) and the azimuthal mode number ( $m$ ) as depicted in Fig. 10 (a). The resonance frequencies of the first two fundamental modes [highlighted with dashed box in Fig. 10 (a)] are evaluated for different azimuthal number. The mode spectrum of the liquid resonator is illustrated in Fig. 10 (b). The amplitudes are scaled to resemble the experimental results presented in Fig. 6. The free spectral range is the characteristic mode spacing for one mode family - our simulation shows an FSR of 0.7068 and 0.7067 nm for the two first modes. The resonance shift reveals a similar power dependency with respect to the actuating voltages with a 1.44 nm shift between 0 to 35 V. The resonance positions of the first two modes with no applied voltage are 771.647 and 771.769 nm in the simulation, while the experimental peaks are at 771.693 and 771.822. The spacing between the TE and TM modes is 0.122 and 0.129 nm for the simulation and experiment, respectively. The small difference between the resonance peaks positions and the experimentally observed resonances is caused by the variation in the refractive index of the liquids. Lastly, the resonance modes that we experimentally observed have been identified using 2D axisymmetric finite element modeling in COMSOL Multiphysics. Our simulations are in excellent agreement with the experimental results, verifying the large resonance shift in the transmission spectra due to electrowetting tuning of the liquid resonator.

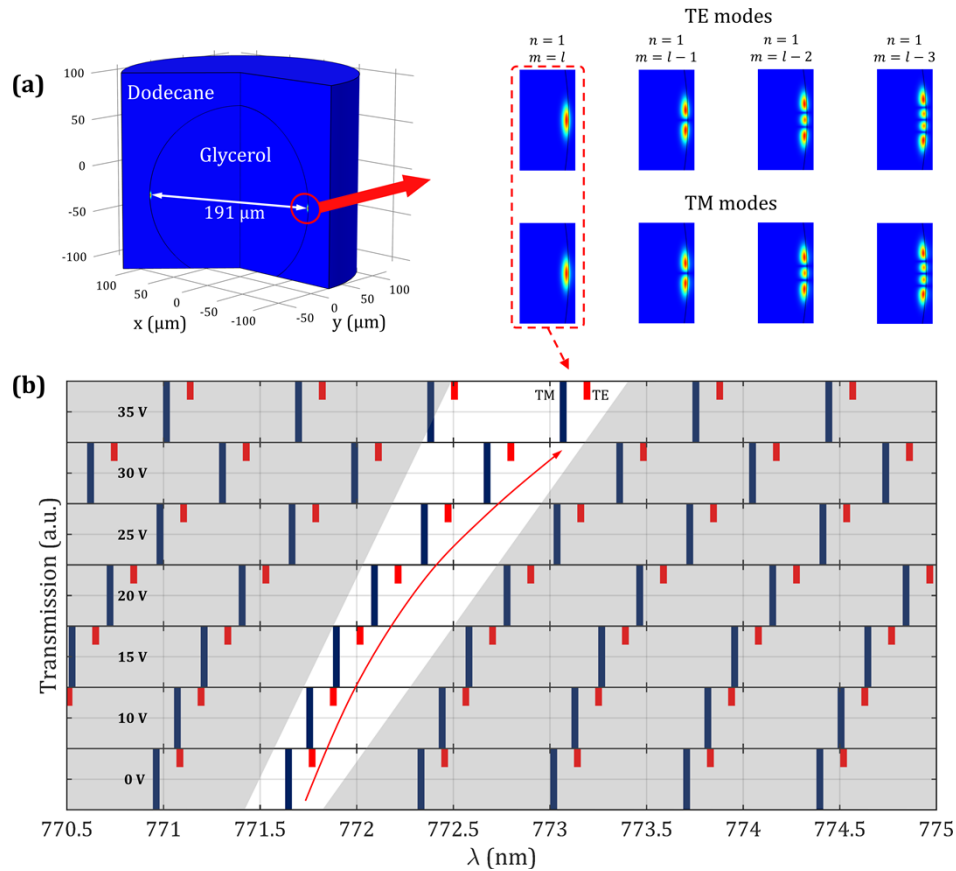


**Fig. 10.** (a) A two-dimensional axisymmetric simulation is performed on the liquid WGM resonator by combining the laminar-two phase liquid flow with wave optics module in COMSOL Multiphysics. A liquid glycerol droplet with a radius of  $95.5 \mu\text{m}$  surrounded in a dodecane bath is simulated. The refractive index of both liquids is obtained by fitting to the Sellmeier equation. The intensity distribution of the mode profile for various polar modes for TE and TM modes is shown here. The color represents electric field of the optical mode.  $n$  is the radial mode number, while  $m$  and  $l$  correspond to the azimuthal and polar mode number, respectively. (b) We have evaluated the resonance frequency of the two fundamental modes (red dashed box) for various actuation voltages resulting in wetting of the liquid droplet. The corresponding resonance wavelength is plotted as a function of actuating voltages. The amplitude of the resonance peak is arbitrary scaled to resemble the experimental results. The simulation shows a quadratic wavelength increase with higher actuating voltages. This agrees with the experimental results presented in Fig. 6 with the FSR of  $\sim 0.7 \text{ nm}$  and maximum resonance shift of  $1.44 \text{ nm}$  at  $35 \text{ V}$ .

## 6. Conclusion

In summary, we have demonstrated a new platform which integrates a liquid microresonator into a chip- scaled device. The device is fabricated using standard microfabrication techniques which opens new possibility of integrating additional photonic components. The device demonstrated resonance modes of  $10^5$  Q-factor in the glycerol-hexane liquid system. Higher Q-factor resonance modes observed thermal capillary noise which randomly excites the resonance resulting in linewidth broadening in both up and down scans. Sensitivity of the liquid resonator to fluctuating environmental factors can be mitigated with an immiscible surrounding liquid and eventually with a fully packaged device. Using the electrowetting-on-dielectric effect, large spectral tuning is achieved by altering the diameter of the droplet. We have shown a maximum tuning range of 1.44 nm by applying 35 V, which exceeds the resonator's FSR (0.679 nm), allowing any resonance modes to be accessed. A geometric analysis of the spectral tuning is derived, showing good agreement to the experimental observations which is reaffirmed later through finite element analysis simulations. Tuning speed of  $\sim 20$  nm/s with a 5 pm precision is achievable with the current design. The chip based liquid resonator presented has great potential as tunable microlasers or a high sensitivity mechanical/biochemical sensor.

**Funding.** University of Colorado Boulder QuEST (Quantum Explorations in Science and Technology) seed grant;; Army Research Office (W911NF1910437); Office of Naval Research (N00014-15-1-2739, N00014-19-1-2251, N00014-19-1-2382, N00014-20-1-20817); Air Force Office of Scientific Research (FA9550-19-1-0364); United States-Israel Binational Science Foundation (2020683); Israel Science Foundation (1572/15, 1802/12, 537/20).

**Acknowledgment.** This research was supported in part by the Colorado Shared Instrumentation in Nanofabrication and Characterization (COSINC); the COSINC-CHR (Characterization) and/or CONSINC-FAB (Fabrication), College of Engineering & Applied Science, University of Colorado Boulder. The authors thank Dr. Omkar Supekar and Dr. Scott Papp for insightful discussions. This research was supported by the United States-Israel Binational Science Foundation (BSF) (Grant No. 2020683) and the Israeli Science Foundation (Grant Nos. 1572/15, 537/20, and 1802/12).

**Disclosures.** The authors declare no conflicts of interest.

**Data availability.** Data underlying the results presented in this paper are not publicly available at this time but may be obtained from the authors upon reasonable request.

**Supplemental document.** See [Supplement 1](#) for supporting content.

## References

1. M. R. Foreman, J. D. Swaim, and F. Vollmer, "Whispering gallery mode sensors," *Adv. Opt. Photonics* **7**(2), 168–240 (2015).
2. M. R. Foreman, S. Avino, R. Zullo, H. P. Looock, F. Vollmer, and G. Gagliardi, "Enhanced nanoparticle detection with liquid droplet resonators," *Eur. Phys. J. Spec. Top.* **223**(10), 1971–1988 (2014).
3. L. Garnier, H. Lhermite, V. Vié, O. Pin, Q. Liddell, H. Cormerais, E. Gaviot, and B. Bêche, "Monitoring the evaporation of a sessile water droplet by means of integrated photonic resonator," *J. Phys. D: Appl. Phys.* **53**(12), 125107 (2020).
4. K. A. Wilson, C. A. Finch, P. Anderson, F. Vollmer, and J. J. Hickman, "Whispering gallery mode biosensor quantification of fibronectin adsorption kinetics onto alkylsilane monolayers and interpretation of resultant cellular response," *Biomaterials* **33**(1), 225–236 (2012).
5. J. Zhu, Ş. K. Özdemir, L. He, D.-R. Chen, and L. Yang, "Single virus and nanoparticle size spectrometry by whispering-gallery-mode microcavities," *Opt. Express* **19**(17), 16195–16206 (2011).
6. Q.-F. Yang, M.-G. Suh, K. Y. Yang, X. Yi, and K. J. Vahala, "Microresonator Soliton Dual-Comb Spectroscopy," in *Conference on Lasers and Electro-Optics* (OSA, 2017), (6312), p. SM4D.4.
7. P. Del'Haye, A. Schliesser, O. Arcizet, T. Wilken, R. Holzwarth, and T. J. Kippenberg, "Optical frequency comb generation from a monolithic microresonator," *Nature* **450**(7173), 1214–1217 (2007).
8. S. B. Papp, K. Beha, P. Del'Haye, F. Quinlan, H. Lee, K. J. Vahala, and S. A. Diddams, "Microresonator frequency comb optical clock," *Optica* **1**(1), 10–14 (2014).
9. Y. H. Lai, Y. K. Lu, M. G. Suh, Z. Yuan, and K. Vahala, "Observation of the exceptional-point-enhanced Sagnac effect," *Nature* **576**(7785), 65–69 (2019).
10. J. Li, M.-G. Suh, and K. Vahala, "Microresonator Brillouin gyroscope," *Optica* **4**(3), 346–348 (2017).
11. C. C. Lam, P. T. Leung, and K. Young, "Explicit asymptotic formulas for the positions, widths, and strengths of resonances in Mie scattering," *J. Opt. Soc. Am. B* **9**(9), 1585–1592 (1992).
12. S. Schiller, "Asymptotic expansion of morphological resonance frequencies in Mie scattering," *Appl. Opt.* **32**(12), 2181–2185 (1993).

13. J. M. Ward, Y. Wu, and S. Nic Chormaic, "Thermo-optical tuning of whispering gallery modes in erbium doped microspheres," *Micro-Optics* **7716**, 77162N (2010).
14. S. L. McCall, A. F. J. Levi, R. E. Slusher, S. J. Pearton, and R. A. Logan, "Whispering-gallery mode microdisk lasers," *Appl. Phys. Lett.* **60**(3), 289–291 (1992).
15. S. Yang, V. D. Ta, Y. Wang, R. Chen, T. He, H. V. Demir, and H. Sun, "Reconfigurable Liquid Whispering Gallery Mode Microlasers," *Sci. Rep.* **6**(1), 1–9 (2016).
16. S. Maayani and T. Carmon, "Droplet Raman laser coupled to a standard fiber," *Photonics Res.* **7**(10), 1188–1192 (2019).
17. A. A. Savchenkov, A. B. Matsko, D. Strelakov, V. S. Ilchenko, and L. Maleki, "Mode filtering in optical whispering gallery resonators," *Electron. Lett.* **41**(8), 495–497 (2005).
18. F. Monifi, J. Friedlein, Ş. K. Özdemir, and L. Yang, "A robust and tunable add-drop filter using whispering gallery mode microtoroid resonator," *J. Lightwave Technol.* **30**(21), 3306–3315 (2012).
19. F. C. Blom, D. R. van Dijk, H. J. W. M. Hoekstra, A. Driessen, and T. J. A. Popma, "Experimental study of integrated-optics microcavity resonators: toward an all-optical switching device," *Appl. Phys. Lett.* **71**(6), 747–749 (1997).
20. V. S. Ilchenko and A. B. Matsko, "Optical resonators with whispering-gallery modes - Part II: Applications," *IEEE J. Sel. Top. Quantum Electron.* **12**(1), 15–32 (2006).
21. M. Sumetsky, Y. Dulashko, and R. S. Windeler, "Super free spectral range tunable optical microbubble resonator," *Opt. Lett.* **35**(11), 1866–1868 (2010).
22. D. V. Strelakov, C. Marquardt, A. B. Matsko, H. G. L. Schwefel, and G. Leuchs, "Nonlinear and quantum optics with whispering gallery resonators," *J. Opt.* **18**(12), 123002 (2016).
23. M. Pöllinger, D. O'Shea, F. Warken, and A. Rauschenbeutel, "Ultrahigh-Q Tunable Whispering-Gallery-Mode Microresonator," *Phys. Rev. Lett.* **103**(5), 053901 (2009).
24. Z.-H. Zhou, C.-L. Zou, Y. Chen, Z. Shen, G.-C. Guo, and C.-H. Dong, "Broadband tuning of the optical and mechanical modes in hollow bottle-like microresonators," *Opt. Express* **25**(4), 4046–4053 (2017).
25. A. Di Falco and G. Assanto, "Tunable wavelength-selective add-drop in liquid crystals on a silicon microresonator," *Opt. Commun.* **279**(1), 210–213 (2007).
26. C. Yang, H. Zhang, B. Liu, S. Lin, Y. Li, and H. Liu, "Electrically tunable whispering gallery mode microresonator based on a grapefruit-microstructured optical fiber infiltrated with nematic liquid crystals," *Opt. Lett.* **42**(15), 2988–2991 (2017).
27. M. Humar, M. Ravnik, S. Pajk, and I. Muševič, "Electrically tunable liquid crystal optical microresonators," *Nat. Photonics* **3**(10), 595–600 (2009).
28. D. Armani, B. Min, A. Martin, and K. J. Vahala, "Electrical thermo-optic tuning of ultrahigh-Q microtoroid resonators," *Appl. Phys. Lett.* **85**(22), 5439–5441 (2004).
29. H.-M. Tzeng, K. F. Wall, M. B. Long, and R. K. Chang, "Evaporation and condensation rates of liquid droplets deduced from structure resonances in the fluorescence spectra," *Opt. Lett.* **9**(7), 273–275 (1984).
30. H.-B. Lin, A. L. Huston, B. L. Justus, and A. J. Campillo, "Some characteristics of a droplet whispering-gallery-mode laser," *Opt. Lett.* **11**(10), 614–616 (1986).
31. A. Biswas, R. G. Pinnick, H. Latifi, and R. L. Armstrong, "Time-resolved spectroscopy of laser emission from dye-doped droplets," *Opt. Lett.* **14**(4), 214–216 (1989).
32. A. Chiasera, Y. Dumeige, P. Féron, M. Ferrari, Y. Jestin, G. N. Conti, S. Pelli, S. Soria, and G. C. Righini, "Spherical whispering-gallery-mode microresonators," *Laser Photonics Rev.* **4**(3), 457–482 (2010).
33. A. Giorgini, S. Avino, P. Malara, P. De Natale, and G. Gagliardi, "Fundamental limits in high-Q droplet microresonators," *Sci. Rep.* **7**(1), 41997 (2017).
34. A. Jonáš, Y. Karadag, M. Mestre, and A. Kiraz, "Probing of ultrahigh optical Q-factors of individual liquid microdroplets on superhydrophobic surfaces using tapered optical fiber waveguides," *J. Opt. Soc. Am. B* **29**(12), 3240–3247 (2012).
35. A. Kiraz, S. Ç. Yavuz, Y. Karadağ, A. Kurt, A. Sennaroglu, and H. Çankaya, "Large spectral tuning of liquid microdroplets standing on a superhydrophobic surface using optical scattering force," *Appl. Phys. Lett.* **91**(23), 231102 (2007).
36. S. Maayani, L. L. Martin, and T. Carmon, "Water-walled microfluidics for high-optical finesse cavities," *Nat. Commun.* **7**(1), 10435 (2016).
37. S. Avino, A. Krause, R. Zullo, A. Giorgini, P. Malara, P. De Natale, H. P. Loock, and G. Gagliardi, "Direct sensing in liquids using whispering-gallery-mode droplet resonators," *Adv. Opt. Mater.* **2**(12), 1155–1159 (2014).
38. J. A. Sofi and S. Dhara, "Stability of liquid crystal micro-droplets based optical microresonators," *Liq. Cryst.* **46**(4), 629–639 (2019).
39. M. W. Royal, N. M. Jokerst, and R. B. Fair, "Droplet-based sensing: Optical microresonator sensors embedded in digital electrowetting microfluidics systems," *IEEE Sens. J.* **13**(12), 4733–4742 (2013).
40. M. Hossein-Zadeh and K. J. Vahala, "Free ultra-high-Q microtoroid: a tool for designing photonic devices," *Opt. Express* **15**(1), 166–175 (2007).
41. A. Kiraz, Y. Karadağ, S. Ç. Yorulmaz, and M. Muradoğlu, "Large spectral tuning of liquid microdroplets by local heating with a focused infrared laser," *Proc. SPIE* **7038**, 70381I (2008).

42. M. Zhang, J. Liu, W. Cheng, J. Cheng, and Z. Zheng, "A Tunable Optical Bragg Grating Filter Based on the Droplet Sagging Effect on a Superhydrophobic Nanopillar Array," *Sensors* **19**(15), 3324 (2019).
43. A. Kiraz, A. Jonáš, M. Aas, Y. Karadag, O. Brzobohatý, J. Ježek, Z. Pilát, P. Zemánek, S. Anand, and D. McGloin, "Droplet resonator based optofluidic microlasers," *Proc. SPIE* **8960**, 896015 (2014).
44. D. Psaltis, S. R. Quake, and C. Yang, "Developing optofluidic technology through the fusion of microfluidics and optics," *Nature* **442**(7101), 381–386 (2006).
45. A. Braslau, M. Deutsch, P. S. Pershan, A. H. Weiss, J. Als-Nielsen, and J. Bohr, "Surface roughness of water measured by x-ray reflectivity," *Phys. Rev. Lett.* **54**(2), 114–117 (1985).
46. D. Baratian, A. Cavalli, D. Van Den Ende, and F. Mugele, "On the shape of a droplet in a wedge: New insight from electrowetting," *Soft Matter* **11**(39), 7717–7721 (2015).
47. J. Kher-Alden, S. Maayani, L. L. Martin, M. Douvidzon, L. Deych, and T. Carmon, "Microspheres with Atomic-Scale Tolerances Generate Hyperdegeneracy," *Phys. Rev. X* **10**(3), 31049 (2020).
48. N. R. Smith, L. Hou, J. Zhang, and J. Heikenfeld, "Experimental Validation of >1 kHz Electrowetting Modulation," *IEEE 17th Biennial University/Government/Industry Micro/Nano Symposium* pp. 11–14 (2008).
49. S. Kuiper and B. H. W. Hendriks, "Variable-focus liquid lens for miniature cameras," *Appl. Phys. Lett.* **85**(7), 1128–1130 (2004).
50. A. K. Mallik, D. Liu, V. Kavungal, Q. Wu, G. Farrell, and Y. Semenova, "Agarose coated spherical micro resonator for humidity measurements," *Opt. Express* **24**(19), 21216–21227 (2016).
51. S. Maayani, L. L. Martin, S. Kaminski, and T. Carmon, "Cavity optocapillaries," *Optica* **3**(5), 552–555 (2016).
52. A. Lee, P. Zhang, Y. Xu, and S. Jung, "Radiation pressure-induced nonlinearity in a micro-droplet," *Opt. Express* **28**(9), 12675–12687 (2020).
53. R. Dahan, L. L. Martin, and T. Carmon, "Droplet optomechanics," *Optica* **3**(2), 175–178 (2016).
54. M. Hossein-Zadeh and K. J. Vahala, "Fiber-taper coupling to Whispering-Gallery modes of a droplet resonator embedded in a liquid medium," *Conf. Lasers Electro-Optics 2006 Quantum Electron. Laser Sci. Conf. CLEO/QELS* **14**(22), 10800–10810 (2006).
55. A. Kiraz, Y. Karadağ, and A. F. Coskun, "Spectral tuning of liquid microdroplets standing on a superhydrophobic surface using electrowetting," *Appl. Phys. Lett.* **92**(19), 191104 (2008).
56. D. Klarman, D. Andelman, R. Aviv, T. Aviv, and M. Urbakh, "A model of electrowetting, reversed electrowetting, and contact angle saturation," *Langmuir* **27**(10), 6031–6041 (2011).
57. F. Mugele and J. C. Baret, "Electrowetting: From basics to applications," *J. Phys.: Condens. Matter* **17**(28), R705–R774 (2005).
58. P. Sen and C. J. Kim, "A fast liquid-metal droplet microswitch using EWOD-driven contact-line sliding," *J. Microelectromechanical Syst.* **18**(1), 174–185 (2009).
59. T. H. Hsu, J. A. Taylor, and T. N. Krupenkin, "Energy harvesting from aperiodic low-frequency motion using reverse electrowetting," *Faraday Discuss.* **199**, 377–392 (2017).
60. X. Song, H. Zhang, D. Li, Q. Jin, D. Jia, T. Liu, and C. Wang, "Liquid Lens with Large Focal Length Tunability Fabricated in a Polyvinyl Chloride/Dibutyl Phthalate Gel Tube," *Langmuir* **36**(6), 1430–1436 (2020).
61. M. Zohrabi, W. Y. Lim, V. M. Bright, and J. T. Gopinath, "High extinction ratio, low insertion loss, optical switch based on an electrowetting prism," *Opt. Express* **28**(5), 5991–6001 (2020).
62. W. J. J. Welters and L. G. J. Fokkink, "Fast electrically switchable capillary effects," *Langmuir* **14**(7), 1535–1538 (1998).
63. J. A. M. Sondag-Huethorst and L. G. J. Fokkink, "Potential-Dependent Wetting of Electroactive Ferrocene-Terminated Alkanethiolate Monolayers on Gold," *Langmuir* **10**(11), 4380–4387 (1994).
64. G. Schweiger and M. Horn, "Effect of changes in size and index of refraction on the resonance wavelength of microspheres," *J. Opt. Soc. Am. B* **23**(2), 212–217 (2006).
65. Y. Ren, M. Li, S. Ray, B. J. Bozeat, and Y. Liu, "Highly accessible low-loss fiber tapering by the ceramic housed electric furnace (CHEF) and frequency-domain real-time monitoring," *Rev. Sci. Instrum.* **92**(3), 1–14 (2021).
66. S. Balac, "WGMode: A Matlab toolbox for whispering gallery modes volume computation in spherical optical micro-resonators," *Comput. Phys. Commun.* **243**, 121–134 (2019).
67. B. E. Little, J. P. Laine, and H. A. Haus, "Analytic theory of coupling from tapered fibers and half-blocks into microsphere resonators," *J. Lightwave Technol.* **17**(4), 704–715 (1999).
68. K. H. Kim, G. Bahl, W. Lee, J. Liu, M. Tomes, X. Fan, and T. Carmon, "Cavity optomechanics on a microfluidic resonator with water and viscous liquids," *Light Sci. & Appl.* **2**(11), e110 (2013).
69. Y. Liu, R. Difoggio, K. Sanderlin, L. Perez, and J. Zhao, "Measurement of density and viscosity of dodecane and decane with a piezoelectric tuning fork over 298–448 K and 0.1–137.9 MPa," *Sens. Actuators, A* **167**(2), 347–353 (2011).
70. J. B. Segur and H. E. Oderstar, "Viscosity of Glycerol and Its Aqueous Solutions," *Ind. Eng. Chem.* **43**(9), 2117–2120 (1951).
71. S. B. Gorajoobi, G. S. Murugan, and M. N. Zervas, "Efficient excitation and phase matching of fiber-coupled degenerate whispering gallery modes," *J. Opt. Soc. Am. B* **36**(9), 2452–2460 (2019).
72. T. Carmon, L. Yang, and K. J. Vahala, "Dynamical thermal behavior and thermal self-stability of microcavities," *Opt. Express* **12**(20), 4742–4750 (2004).



73. M. L. Gorodetsky and V. S. Ilchenko, "Optical microsphere resonators: optimal coupling to high-Q whispering-gallery modes," *J. Opt. Soc. Am. B* **16**(1), 147–154 (1999).
74. I. V. Blazhnov, N. P. Malomuzh, and S. V. Lishchuk, "Temperature dependence of density, thermal expansion coefficient and shear viscosity of supercooled glycerol as a reflection of its structure," *J. Chem. Phys.* **121**(13), 6435–6441 (2004).
75. Z. Cao, L. Jiang, S. Wang, M. Wang, D. Liu, P. Wang, F. Zhang, and Y. Lu, "All-glass extrinsic Fabry–Perot interferometer thermo-optic coefficient sensor based on a capillary bridged two fiber ends," *Appl. Opt.* **54**(9), 2371–2375 (2015).
76. Metricon, "Model 2010/M Overview," <https://www.metricon.com/model-2010-m-overview>.
77. J. Rheims, J. Köser, and T. Wriedt, "Refractive-index measurements in the near-IR using an Abbe refractometer," *Meas. Sci. Technol.* **8**(6), 601–605 (1997).
78. O. D. Supekar, M. Zohrabi, J. T. Gopinath, and V. M. Bright, "Enhanced Response Time of Electrowetting Lenses with Shaped Input Voltage Functions," *Langmuir* **33**(19), 4863–4869 (2017).